Assessment pebble virtual velocity from combined active RFID fixed stations and geophones

Authors

Mathieu Cassel[a], Oldrich Navratil[b], Frédéric Liébault[c], Alain Recking[c], Daniel Vázquez-Tarrío[d], Maarten Bakker[e], Sébastien Zanker[f], Clément Misset[g], Hervé Piégay[a]

[a] University of Lyon, UMR 5600 CNRS-Environnement Ville Société, ENS de Lyon, 15 Parvis René Descartes, Lyon Cedex,

[b] University of Lyon, UMR 5600 CNRS-Environnement Ville Société, University Lumière Lyon 2, 5 avenue Pierre Mendès-France, Bron Cedex, F-69635, France

[c] Université Grenoble Alpes, INRAE, ETNA, 38000 Grenoble, France

[d] Geological Hazards Division, Spain Geological Survey (IGME), 28003 Madrid, Spain

[e] Univ. Grenoble Alpes, CNRS, IRD, Grenoble INP, IGE, 38000 Grenoble, France

[f] EDF, DTG, Grenoble, France

[g] ONF-RTM, Northern Alps Agency, Chambéry, France

Abstract

The monitoring of coarse sediment transport is a domain teeming with technical innovations and methodological developments aimed at improving the characterization of bedload processes at different spatial and temporal scales. Radio frequency identification (RFID) technology has improved sediment tracking experiments, allowing the characterization of processes at the individual particle and flood-event scales. Meanwhile, geophone sensors have enabled the continuous monitoring of bedload intensity and variations in sediment fluxes at intra-flood event and sediment-pulse scales. The combination of these two techniques allows these scales and processes to be linked. In this study, we used a combination of active ultra-high frequency RFID and geophone stations to link the virtual velocity of tracers with channel geophone activity, hydraulic forcing, and tracked particle properties, analyzing the results with single and multiple regression models. Our results show that compared with discharge or stream power, the geophone activity best explained the variance (81%) of the virtual velocity observed. Furthermore, when all the control variables tested were combined in an empirical model, the model explained 95% of this variance, and allowed quantification of the portions of the

variance explained by hydraulic forcing, geophonic activity, and tracked particles. This shows the high potential of such monitoring combinations for future in-field experiments to investigate bedload processes in river systems of different morphologies at different spatiotemporal scales.

1. Introduction

Although bedload transport processes are important in flood hazard assessment, engineering applications, and river ecology, our understanding of these processes remains limited, making them difficult to predict (Ancey, 2020a, 2020b).

The movement of individual coarse sediment particles depends on hydraulic forcing, river system morphodynamics, channel geometry, and particle properties (Hassan and Bradley, 2017; Vázquez-Tarrío and Batalla, 2019). The effects of these factors on particle motion have been investigated using stochastic and deterministic approaches (Cassel et al., 2021a) involving sediment tracers or smart pebbles consisting of sediment particles, either natural or artificial, equipped with various types of sensors or transmitters (Hassan and Roy, 2016). The stochastic approach is used to analyze the motion of actual particles, distinguishing phases of displacement and rest quantified by hop length and duration, and to compute probability curves for both of these phases (Einstein, 1937; Ergenzinger and Schmidt, 1990; Habersack, 2001; Olinde and Johnson, 2015). The deterministic approach considers flow discharge and stream power above the critical level that allows the transport of particles of a given size (Shields, 1936; Bagnold, 1966). Following this approach, many studies have developed models for the barycenter of downstream particle progression (Arnaud et al., 2017; Chardon et al., 2021), dispersion (Haschenburger, 2013), and virtual velocity (Haschenburger and Church, 1998; Liébault et al., 2012) as a function of excess stream power (Lamarre and Roy, 2008; Schneider et al., 2014; Houbrechts et al., 2015; Arnaud et al., 2017; Rainato et al., 2020; Chardon et al., 2021) or stream impulse (Bradley, 2017; Gilet et al., 2020; Imhoff and Wilcox, 2016; Phillips et al., 2013; Phillips and Jerolmack, 2014). Recent meta-analysis-based investigations have pointed towards the important role of the channel morphology and dimensions (Vázquez-Tarrío et al., 2018; Vázquez-Tarrío and Batalla, 2019), and have quantified the variance in travel distance explained by these factors. However, small-scale turbulent flow processes and grain-grain interactions also remain of fundamental importance in bedload transport (Frey and Church, 2011), and their effects on tracer transport have not yet been investigated in a field experiment. Assuming that grain–grain (mobile vs. mobile particles) and grain–bed (mobile vs. immobile particles) interactions (*i.e.* collisions) are colinear and generate ground vibrations, seismic activity could be used to monitor these interactions (Tsai et al. 2012).

The field monitoring of bedload transport remains challenging, whether in coarse-bedded gravel rivers, steep-slope torrents (Rickenmann, 2017), or large rivers during rare and intense flood events, and the development of new tools and methods is important to gain insight into the contributions of the different controlling factors (Kondolf and Piégay, 2016). Among the recent field monitoring developments, active ultra-high frequency tracers (a-UHF tracers) and seismic sensors (SS) are highly complementary, allowing the comprehensive monitoring of bedload transport and the different controlling factors (*i.e.* bedload properties and hydraulic conditions) affecting its dynamics.

Over the last few decades, RFID technology with wireless detection of individual (buried or immersed) transponder-equipped particles has been used to investigate the transport distance between tracers' positions before and after flood events (Schneider et al., 2014; Chapuis et al., 2015; Arnaud et al., 2017; Misset et al., 2020a; Chardon et al., 2021) and the virtual velocities of particles (Liébault et al., 2012; Milan, 2013; Mao et al., 2017; Brenna et al., 2019; Rainato et al., 2020; Cassel et al., 2021b; Oss Cazzador et al., 2021). The earliest in-field experiments using stationary antennas for detection of RFIDs (Schneider et al., 2010; Mao et al., 2017; Stähly et al., 2020) used only low frequency passive transponders (PIT tags) and reported low recovery rates; however, recent developments using sediment tracers equipped with a-UHF tags have shown encouraging results in rivers with very active bedload transport (Brousse et al., 2020b, 2020a; Cassel et al., 2020; Misset et al., 2020a). Additionally, such a-UHF tags were recently monitored by Cassel et al. (2021b) using an autonomous stationary antenna system (named e-RFIDuino) to measure particle virtual velocity during flood events, observations that are analyzed in this paper. Furthermore, the signals of a-UHF tags equipped with a movement sensor sensed by the e-RFIDuino system could facilitate observation of particle movements without displacement along the channel. Such movements were first reported in the second half of the 20th century (Stevens, 1969; Urbonas, 1968; both in Schumm and Stevens, 1973), but in-field investigations of them remain scarce (Olinde and Johnson, 2015).

Geophones installed on river banks can be used to monitor bedload transport as they can record the seismic activity generated at the river bed. Bedload flux can be estimated from seismic power (Tsai et al., 2012), when taking into account both contributions of water turbulence and of bedload flux (Dietze et al., 2019), when linking grain-scale impacts with seismic activity (Gimbert et al., 2019), or performing in-field validations to estimate absolute bedload transport rates (Bakker et al., 2020; Dietze et al., 2020). This monitoring approach is particularly suitable for investigating processes of high temporal variability, as it can run quasi-continuously over a long period of time and can operate in high-magnitude flow events during which in-stream equipment is likely to break or fail to function correctly. Bedload samples are always necessary to calibrate the seismic records when investigating the absolute bedload transport flux (Rickenmann et al., 2014; Antoniazza et al., 2020; Bakker et al., 2020), and these may be acquired with sediment traps or basket samplers (e.g. Helley Smith). Geophones have been used to study glacial lake outbursts (Cook et al., 2018), debris flow triggering in torrents (Navratil et al., 2013; Bel et al., 2017; Roth et al., 2017), gravel mobilization (Schmandt et al., 2017), and bedload transport downstream of hydropower dams (Aigner et al., 2017) and in near-natural Alpine streams (Misset et al., 2020a). Such programs often combine geophone sensors with other measurements such as turbidity (Misset et al., 2020b), flow rheological characterization (Navratil et al., 2013), rainfall (Bel et al., 2017), topographic survey (Schmandt et al., 2017; Cook et al., 2018), and bedload flux samples (Rickenmann et al., 2012; Aigner et al., 2017; Misset et al., 2020a), but only rarely do they include sediment tracers (Habersack et al., 2010; Schneider et al., 2014; Misset et al., 2020a).

a-UHF tracers and geophones are monitoring techniques associated with two very distinct and classical formalisms in physics: Lagrangian and Eulerian formalisms. The approach used to track individual particles during their movement in a river using a-UHF tracers is based on a Lagrangian formalism. The seismic approach using geophones to estimate bedload transport over a river section is based on a Eulerian formalism. From technical considerations, it is essential to combine these two formalisms to better understand the complexity of bedload processes and how the dynamics of individual particles add up to bedload dynamics in rivers. Thus, a-UHF tracers can help in the calibration of geophones, and geophones can improve the interpretation of tracer displacements. Indeed, the seismic activity generated during floods can allow monitoring of the entire population of coarse sediment particles. Thus, the combination of these two techniques, which has not yet been studied in detail, is of great interest.

In this study, we sought to investigate the potential of a newly-conceived fixed monitoring station installed along a confined Alpine stream channel. This monitoring station was designed to detect both particle movement from the timing and signal strength of passing coarse sediment particles equipped with a-UHF tags, and bedload flux from a set of geophones. The particle movement was quantified through the individual tracer virtual velocity (Haschenburger and Church, 1998), which is defined as the transport distance divided by the measurement interval. The data were analyzed in connection with the seismic activity measurements, to link tracer movements to flow discharge, tracer properties (shape, mass, and past activity), and bedload transport conditions. Our main goals were: (1) to explore the potential of the combination of these two distinct monitoring methods (a-UHF RFID and geophones); (2) to compare the respective influences of the above mentioned three main controlling factors; (3) to investigate the accuracy of predictions of the virtual velocity of tracers according to these controlling factors using a least squares multiple regression empirical model; and finally, (4) to test the potential of a-UHF tracers with motion detectors for future investigations on particle dynamics.

2. Study Site

The Séveraisse River drains a watershed with little human impact in the Ecrins Massif in the French Alps. It has a catchment area of about 223 km² (maximum elevation of 3579 m a.s.l.; minimum elevation of 780 m a.s.l.) and a length of 33.2 km. Along its course, it shows several sequences of well-developed braided reaches in wider sections of the valley, and straight (confined) single-thread reaches in the more laterally-confined sections (Misset et al., 2020a). The upper part of the catchment is highly erosive, and processes such as rock fall, debris flows, and sediment transport from torrents deliver large amounts of sediment to the main channel. From late spring to the beginning of summer, the Séveraisse River exhibits a hydrologic regime characterized by a high-flow period driven by snowmelt, with daily discharge fluctuations capable of transporting bedload material. This is followed, during the late summer and autumn, by generally lower flows generated by ice-melt with occasional storm events that can cause large flood events with intense bedload transport. The lowest flows occur in winter when the basin is covered by snow. In this study, we consider the snow-melt and storm driven events that occurred before and after the 15th of July 2020, respectively, when the discharge base level dropped below 10 $m^3 s^{-1}$.

Our study site is located approximately in the middle section of the river near the village of Villar-Loubière (44°49’28.34’’North; 6°08’56.22’’East), just upstream of a gauging station (Figure 1) installed in 1969, and represents a drainage area of ca. 130 km². In the vicinity of a bridge, the channel is straight, laterally confined, and 13 m wide (Bakker et al., 2020), with an average slope of 0.014 m m^{-1}. The riverbed is armored with cobbles of grain size D50 = 11 cm and D84 = 30 cm, as derived from Wolman pebble counts (Misset et al., 2020a). Under the most frequent hydraulic conditions, the bedload fluxes generated in the upstream braiding are transferred efficiently within this confined section, without morphological adjustments (Misset et al., 2020a). The morphodynamically-active upstream braided reach exhibits a finer grain size with D50 = 28 mm and D84 = 91 mm.

3. Material and Methods

3.1. Bedload monitoring equipment

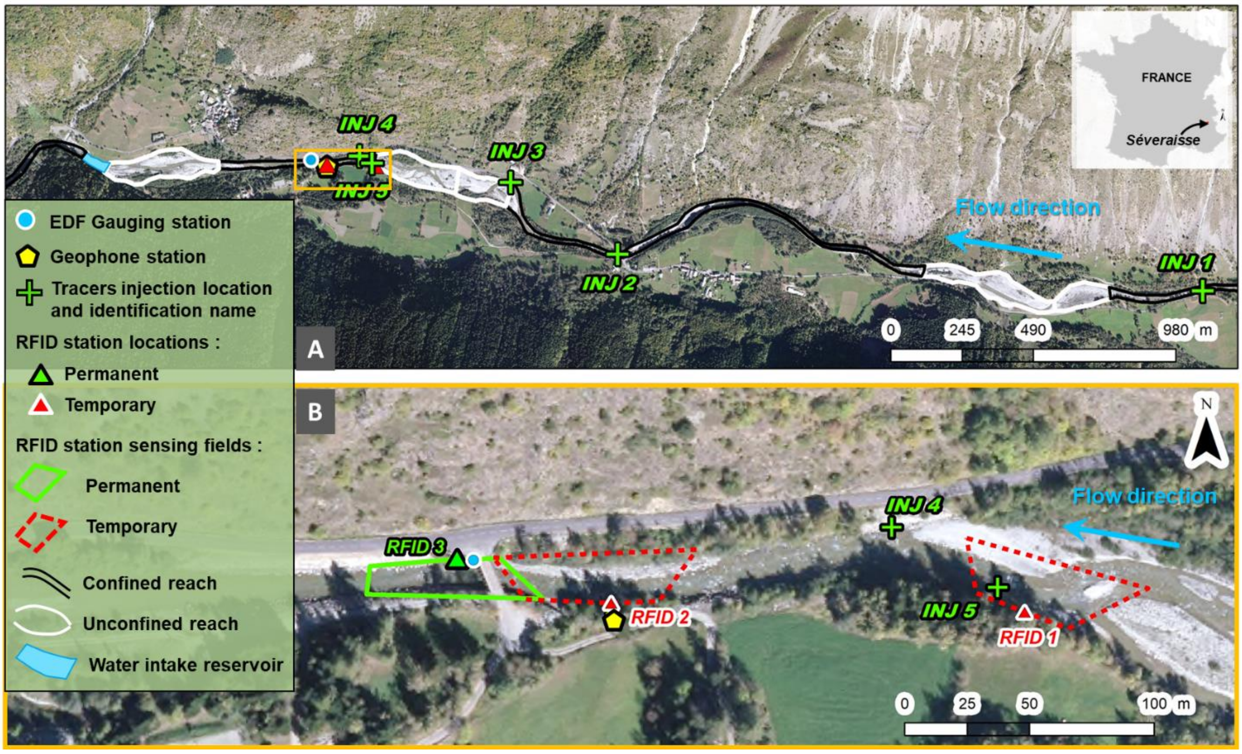

Figure 1. Overview of the Séveraisse River (A) and the monitoring instruments (B).

The bedload monitoring used in this study combines a coarse sediment tracing program using a-UHF equipped tracers with geophone sensors recording vertical ground vibrations. The coarse sediment tracing program was progressively implemented between 2018 and 2020 to quantify the transport and mobility of coarse particles within the braided reach over multiple years (see Misset et al., 2020a). During the 2020 field campaign, the instruments were installed close together (Figure 1b), along a straight confined reach.

3.1.1 Monitoring particle movement

3.1.1.1 Sediment tracers

Over the course of three years, a total of 123 tracers were injected in 10 seeding operations at 5 different locations (Table 1; Figure 1). Because of high water discharges at the seeding periods, the tracer injection procedure consisted of dropping the tracers into the main channel flux, either from bridges (*INJ 1* and *INJ 2*) or from banks (*INJ 3*, *INJ 4* and *INJ 5*). Several tracer inventories performed in 2018 (Misset et al., 2020a) and 2019 revealed that the majority of the tracers seeded in 2018 and 2019 were already located downstream of the reach investigated in this study at the beginning of the 2020 campaign. Four tracer inventories were also performed before (*i1*), during (*i2* and *i3*), and after (*i3*) the monitoring period using stationary antennas: the 26th of May, 22nd of July, 26th of August, and 30th of November 2020, respectively. The results of these inventories are not analyzed in this paper, but they did allow us to know the final position of the tracers that were located upstream of the stationary antenna at the beginning of the monitoring period.

The tracers seeded at the beginning of the 2020 field campaign were artificial stones (Figure 2-A) composed of a mixture of polyurethane resin and corundum (Cassel et al., 2016, 2021a). They were equipped with active transponders of ultra-high frequency (a-UHF tags). The a-UHF tags used in this study were COIN ID and COIN MOV models developed by Ela Innovation® and distributed by Cipam®. These a-UHF tags were chosen because they have a relatively long operating life (up to 5 years), and can be sensed over dozens of meters (up to 40 m) in an open environment and over several meters when buried or immersed (up to 2.6 m). Their beacon signals are emitted at 433.9 MHz and do not suffer from collision when several transponders are simultaneously present in the antenna sensing field. The beacon signal also includes a received signal strength indication (RSSI) (Cassel et al., 2017, 2020). The COIN MOV tags include a movement sensor that directly transmits through the beacon signal, whether or not it has moved since the previous signal emission. Thus, when the COIN MOV transponders are sensed by an antenna, three parameters are provided: the identification (Id) number, the RSSI, and an indication of whether (1 is sent) or not (0 is sent) it has moved since the last beacon signal emission. During the 2020 campaign, 29 tracers equipped with COIN ID tags were seeded, and 5 tracers equipped with COIN MOV tags were tested. The interval between signal emissions was set to 2.2 seconds and 900 ms for tracers equipped with COIN ID and COIN MOV, respectively. The shorter interval used for the COIN MOV tracers was set to acquire more temporal details on RSSI variations and to sense movements as close as possible to the moment of tracer displacement.

Table 1. Summary of the tracer seeding information

Injection ID	ID of Injection location	Date of seeding	Number of tracers injected COIN ID/COIN MOV	D50 (mm)	Number of tracers detected during the 2020 season at RFID stations RFID 3 and RFID 2 (RFID 2 indicated in parentheses)
2	*INJ 1*	03/05/**2019**	20/0	68	2
5	*INJ 2*	27/05/**2020**	9/0	57.3	6
6	*INJ 4* & *INJ 5*	28/05/**2020**	0/2		2
7	*INJ 2*	28/05/2020	10/0		8
8	*INJ 5*	02/06/**2020**	2/1		3 (3)
9	*INJ 5*	03/06/**2020**	3/2		5 (2)
10	*INJ 5*	04/06/**2020**	5/0		5 (1)
				Total	**31 (6)**

Notes: In the rightmost column, the numbers in parentheses indicate the number of tracers sensed by station RFID 2. Injections 1, 3, and 4 are not presented here as the tracers seeded at these injections were either immobile or were already downstream of the reach investigated in this study.

3.1.1.2 Tracer monitoring stations

Three RFID-tracking stations were installed on-site on the 28 of May 2020, two being temporary and one, referred to as “e-RFIDuino”, being permanent (Cassel et al., 2021b) (Figure 1b). When a tracer signal was sensed by an antenna, the three stations recorded its identification number, the RSSI, and the time, plus the movement indication if the tracer was equipped with a COIN MOV tag. After the installation of the stations, their antenna sensing fields were delimited using the procedure detailed in Cassel et al. (2021). This ensured the tracer’s detection over the whole channel width and allowed us to determine the channel length over which the tracers could be monitored. A channel length of ~60 m was obtained for RFID 2 and RFID 3 (Figure 1B).

The two temporary stations consisted of equipment used for mobile prospection surveys (Figure 2-C): a rugged field computer connected to a SCIEL reader equipped with a SLENDER III antenna (see details in Cassel et al., 2017, 2020). The upstream temporary station was installed on the left bank at the location of the *INJ 5* seeding point, and was only used to observe the departure of the tracers seeded at this location and the signal evolution of the COIN MOV tags, which were tested here for the first time. The downstream temporary station was installed as close as possible to the geophone station, and was used to detect the tracers' passages and to monitor their displacement and residency duration within the sensing field. These mobile stations were installed in the morning and removed at night when the tracers were injected at *INJ 4* and *INJ 5*: on the 28th of May and the 2nd, 3rd, and 4th of June.

The e-RFIDuino station consisted of an environmental Arduino based datalogger kitted out with a commercially available RFID reader (SCIEL reader) and a SLENDER III antenna (Figure 2-B; see design details in Cassel et al. 2021). It was installed next to the EDF gauging station (Figure 1b), which provides flow discharge measurements (10-minute time-step recording). The e-RFIDuino station remained on-site during the whole campaign (from the 28th of May until the 26th of October 2020).

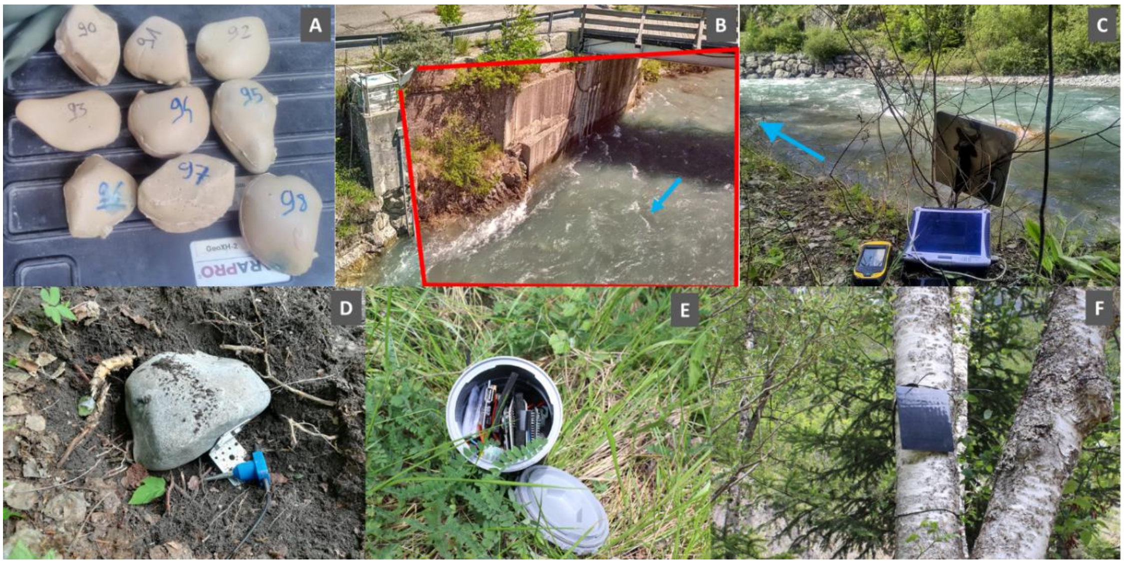

Figure 2. RFID devices, geophone station (A: artificial tracers equipped with a-UHF tags; B: the e-RFIDuino station; C: the mobile station RFID 1) and geophone datalogger (D: the Geospace ® GS-20DX geophone before its installation on a rock; E: the encapsulated datalogger of the geophone signal; R: solar panel).

3.1.2 Geophone monitoring stations

A geophone station was installed in a similar way to that described by Navratil et al. (2013) and Bel et al. (2017). The geophone station was powered by a small 3.7 V battery (10 000 mAh), a solar panel (3 W) and a solar power regulator. The microcontroller (Arduino Mini Pro®; 8 MHz) used was chosen because of its very low energy consumption. An RTC (Real Time Clock controller; RTC DS3231 AT24C32 IIC) and SD card reader (DEV13743) completed the recording system. A micro-SD memory card (8 Go) provided a data storage autonomy of several months. A GS20-DX Geospace® geophone was deployed on the left riverbank ca. 2 m from the river flow. This geophone registers ground velocity in the vertical direction (with a natural frequency of 8 Hz). The vibration frequency typically associated with bedload transport is 50–60 Hz (Bakker et al., 2020), which meant that the maximum recording frequency of the microcontroller (5 Hz) was insufficient to record the signal output of the geophone, *i.e.* a voltage proportional to the soil vibration velocity. To accommodate this problem, the raw geophone signal was first processed with an electronic interface that performed: 1) a signal rectification; 2) low-pass filtering (Frequency = 2.5 Hz); and 3) amplification of the geophone signal output, following the method of Navratil et al. (2013). The output signal was finally recorded at 5 Hz. The offset and gain of this interface can be adjusted to account for local ground properties and the specific location of each geophone. The geophone was fixed on a big boulder embedded in the riverbank (at 20 cm depth in the ground) to reduce the effects of direct impacts of rain, hail, and runoff, and the wires to the solar panel were fixed to eliminate noise induced by wind. Finally, to define a gain value and verify that the station worked properly, preliminary tests were performed with boulders (ca. 10 kg) manually thrown into the river (from 3–4 m in height) and onto the riverbanks (from 1.5 m), and these were clearly identified in the seismic record.

3.2 Data computing

3.2.1 Data compilation

Following Haschenburger and Church (1998), the virtual velocity ($\overline{v}$) of passing tracers expressed in m s^{-1} was computed using the channel length covered by the antenna sensing field, i.e. 60 m (see section *3.1.1.2 Tracer monitoring stations*) divided by the tracer stay duration within the sensing field, which is the difference between the detected time of entry and the time of exit from the antenna sensing field.

To explore the role of factors influencing the virtual velocity of the tracers' passages ($\overline{v}$), we distinguished three types of controlling variables (Table 2): 1) the tracer properties (weight, shape, size) including the transport distance and the time elapsed since tracer injection (*i.e.* past tracer activity); 2) the hydraulic conditions; and 3) the bedload transport conditions.

The tracers' properties were measured before they were seeded in the river. Each tracer was weighed and its three axes were measured. The past tracer activity was measured in a Geographic Information System (travel length along the river thalweg) or calculated using the time of injection and the time of the first detection by the RFID monitoring station when the tracer entered the antenna sensing field (time elapsed since injection).

We used the times of entry into and exit from the antenna sensing field of each tracer to determine the residence time period, for which we also derived: (1) the stream power resulting from flow discharges measured at the gauging station (***Q***, in m^3 s^{-1}); and (2) the seismic activity (***G***, in mV) recorded at the geophone station. Values ***Q*** and ***G*** were both recorded at 10-minute intervals, and their average, range of variation (difference between maximal and minimal values), and standard deviation ($\boldsymbol{\sigma}_{Qi}$ and $\boldsymbol{\sigma}_{Gi}$) were calculated to describe their fluctuations over the residence periods. The maximal values of ***Q*** and ***G*** were also calculated, but their links to virtual velocity were both weaker than those of their average values.

We investigated two stream power formulations commonly used in riverine coarse sediment tracking studies, both of which include the tracer size in the formula:

- the sum of the unit excess flow power based on the discharge values exceeding the critical discharge for bedload transport ($\boldsymbol{Q_c}$), which is also considered as the total excess flow energy (Haschenburger, 2013; Schneider et al., 2014; Chardon et al., 2021);
- and the dimensionless stream power (Eaton and Church, 2011), which allows comparisons between contrasting river systems of different width, slope, and discharge regime, and avoids scale differences (Vázquez-Tarrío et al., 2018). It could thus be a good standard for further replications of the empirical models developed in this study.

The sum of the unit excess flow power ($\sum_{\boldsymbol{h}}^{\boldsymbol{P_i}}(\boldsymbol{\omega_t} - \boldsymbol{\omega_c})$ in W m^{-2}) is suitable when several hydrological events are recorded by displacement of tracers between two surveys, or when the tracer residence duration in the antenna sensing field is long. It is defined for each tracer passage P_i as:

$$\sum_{\boldsymbol{t}}^{\boldsymbol{P_i}}(\boldsymbol{\omega_t} - \boldsymbol{\omega_c}) = \sum_{\boldsymbol{t}}^{\boldsymbol{P_i}} \frac{\boldsymbol{\rho \cdot g \cdot (Q_t - Q_c) \cdot S}}{\boldsymbol{w}} \qquad \textbf{(E1)}$$

where $\boldsymbol{Q_t}$ is the instantaneous discharges summed within the tracers passage $\boldsymbol{P_i}$ to a resolution of one second; $\boldsymbol{S}$ and $\boldsymbol{w}$ are the straight confined channel slope (0.014 m m^{-1}) and width (13 m), respectively; $\boldsymbol{\rho}$ is the water density equal to 1000 kg m^{-3}; and $\boldsymbol{g}$ is the acceleration due to gravity equal to 9.81 m s^{-2}. Bedload had been measured with a Elwha sampler over successive years, and the critical discharge for bed mobility was known to be 11.9 m^3s^{-1} (Bakker et al., 2020). This value is also consistent with the 11.7 m^3 s^{-1} estimated using the following equation derived from the Shields and Manning formulas:

$$Q_c = \left(K \cdot w \cdot S^{1/2}\right) \cdot \left(\left((1.65 \cdot D_{84} \cdot \tau_c^*)/S\right)^{\frac{5}{3}}\right) \qquad \textbf{(E2)}$$

where $\boldsymbol{K}$ is the Manning-Strickler coefficient equal to 26 (calculated using the Strickler (1923) formula: $\boldsymbol{K} = \frac{\boldsymbol{1}}{\boldsymbol{n}} = \frac{\boldsymbol{21}}{\boldsymbol{D_{84}}^{1/6}}$, $\boldsymbol{D_{84}}$ is the 84th percentile of the tracers *b*-axis values (0.303 m), and τ_c^* is the critical Shields number (0.045).

The dimensionless stream power ($\boldsymbol{\omega}^*$) proposed by Eaton and Church (2011) is calculated as:

$$\omega^{*} = \frac{\omega}{\boldsymbol{\rho}\cdot(\boldsymbol{g}\cdot\boldsymbol{R}\cdot\boldsymbol{D})^{3/2}} \qquad \textbf{(E3)}$$

where $\boldsymbol{\omega} = (\boldsymbol{\rho}\cdot\boldsymbol{g}\cdot\boldsymbol{S}\cdot\overline{\boldsymbol{Q}}_{\boldsymbol{i}})/\boldsymbol{w}$ is the unit stream power ($\boldsymbol{\omega}$ in W m^{-2}), as defined by Bagnold (1966, 1980), and estimated at the mean value of the discharge $\overline{\boldsymbol{Q}}_{i}$ observed during the passage of the tracers $\boldsymbol{P_i}$. $\boldsymbol{R}$ is the submerged specific weight of the tracer (1.65), and $\boldsymbol{D_i}$ is the tracer *b*-axis value in m. The dimensionless stream power is linearly dependent on the mean value of the discharge.

As the flow discharge partially drives the bedload transport sensed by a geophone, it may be expected that the dimensionless stream power and seismic values are colinear; we therefore computed the residuals ($\boldsymbol{\varepsilon}_i$) from the linear relationship between the log-transformed mean dimensionless stream power ($\boldsymbol{\omega}^{*}$) and the log-transformed seismic averaged values ($\overline{\boldsymbol{G}}$). By using these residuals together with the mean discharges, we avoided an artificially strong correlation due to collinearity between the two variables.

Table 2. Description of the control factors tested to predict particle virtual velocity.

Factor type	Description	Code Variable	tested in stepwise process
Tracer properties	Tracer b-axis in m	D_i	***Yes***
	Tracer mass in kg	m_i	***Yes***
	Tracer sphericity based on Sneed and Folk (1958) index : $\Psi_i = \sqrt[3]{\frac{c}{ab}}$ with *a*, *b*, and *c* the longest, intermediate, and shortest axes of the tracer.	Ψ_i	***Yes***
Past tracer activity	Travel length in m since tracer injection	L_i	***Yes***
	Time elapsed between tracer injection and its entrance into the antenna sensing field	t_i	***Yes***
Hydrological and hydraulic variables	Water discharge in $m^3\ s^{-1}$. This is the mean value of the discharges measured during the tracer passage.	$\bar{Q}_i$	**No**
	Difference between maximal and minimal discharge values measured during the tracer passage.	Δ_{Qi}	***Yes***

	Standard deviation of the discharge values measured during the tracer passage.	$\boldsymbol{\sigma}_{Qi}$	***Yes***
	Sum of the unit excess flow power in W m^{-2}	$\sum_{h}^{P_i}(\omega_h - \omega_c)$	**No**
	Dimensionless mean stream power	ω^*	***Yes***
Geophonic variables	Average geophone activity observed during the passage of the tracer passage in mV.	$\overline{G}_i$	**No**
	Difference between maximal and minimal seismic values measured during the tracer passage in mV.	Δ_{Gi}	***Yes***
	Standard Deviation of the seismic values measured during the tracer passage in mV.	$\boldsymbol{\sigma}_{Gi}$	***Yes***
	The residuals from the power model linking log transformed dimensionless mean stream power (ω^*) and log transformed seismic averaged values ($\overline{G}$)	ε_i	***Yes***

3.2.2 Data analysis

The acquired data were processed and analyzed using R and Rstudio statistical software (http://www.rstudio.com/). All the variables (virtual velocity and their potential drivers) were log-transformed. We first determined how much of the variance in the virtual velocity of the tracers' passages could be explained by each of the potential drivers in Table 2. Then, the correlations of the averaged seismic activity with the mean flow discharge and the dimensionless stream power were analyzed using multiple R-squared coefficients obtained with the "*lm()*" function in Rstudio. Finally, using all potential drivers, we developed an empirical model to predict the virtual velocity of tracers with the best accuracy and lowest variance. To do this, the drivers were processed using multiple least squares regression in a linearized form (also using the "lm()" function in Rstudio) and a stepwise procedure, as was successfully used by Vázquez-Tarrío and Batalla (2019) to predict tracer transport distances and to investigate the influence of its drivers. This stepwise procedure was performed using the "stepAIC ()" function of the "MASS" package in Rstudio. To assess the potential inflation of variance in the R^2 associated with collinearity between the drivers, we computed the variance inflation factor (VIF), which quantifies how much the variance of an estimated regression coefficient is increased by the driver's collinearity. This was performed using the "vif()" function of the "car" package in Rstudio, and following the methods of previous authors (James et al., 2013; Vázquez-Tarrío and Batalla, 2019) we considered VIF values lower than 10 acceptable.

4. Results

4.1 Observations

Over the total monitoring period, the stations *RFID 3* and *RFID 2* recorded 31 and 6 tracer passages, respectively (Table 1 and Figure 3), with 6 tracers being detected by both RFID stations. Among the 31 tracers detected, 29 were injected in 2020, including 14 injected at *INJ 2* (Fig. 1; 1.2 km upstream of the station *RFID 3*), 14 injected at *INJ 5* (275 m upstream of the permanent RFID station), and 1 injected at *INJ 4* (about 225 m upstream of the RFID stations). Two detected tracers were injected in 2019 at location *INJ 1*, the most upstream point (3.5 km upstream of station *RFID 3*). It should be noted that of the tracers located upstream before the monitoring period and then located downstream in the tracer inventories *i2* to *i4* performed after the monitoring period, all were sensed by the station.

The average *b*-axis, weight, and sphericity of the tracers were 59 mm, 0.265 kg, and 0.73, respectively (Figure 4). The residency durations within the RFID station sensing fields ranged from 36 seconds to 8.8 days, corresponding to virtual velocities of 2.01 m s^{-1} to 7.9e-5 m s^{-1} (*i.e.* 6.8 m day^{-1}), with both extremes being recorded by the permanent station. Of the 37 passages, 26 occurred during snow-melt-driven flood events (before mid-July) with mean discharges ranging from 11.3 m^3 s^{-1} to 22.5 m^3 s^{-1}. The remaining 11 passages occurred during rainfall driven flood events, with mean discharges varying between 6.1 m^3 s^{-1} to 70 m^3 s^{-1} (the latter was observed during the peak of a flood event with an estimated return period of 30-years). The seismic activity recorded during the tracer passages ranged from 0.003 mV to 0.055 mV over periods of snow-melt-driven flows, and from 0.002 mV to 0.27 mV over rainfall-driven flows (Figure 3). Over these two periods, the virtual velocities ranged from 0.007 to 0.095 m s^{-1} for snow-melt driven flows and from 0.002 to 2.01 m s^{-1} for rainfall driven flows. Thus, we observed particle motion under contrasting flow conditions, for different tracer properties, and for different passage velocities.

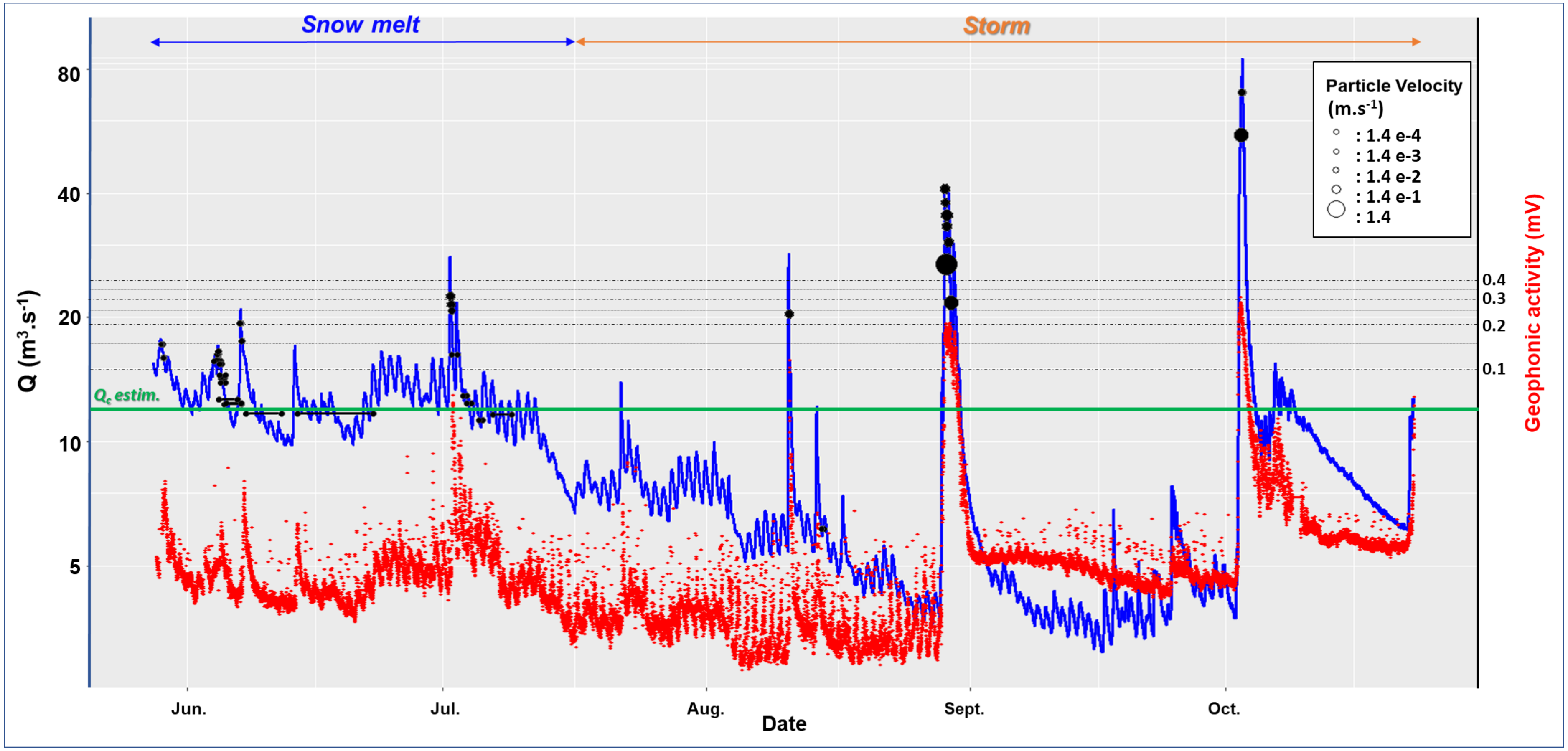

Figure 3. Discharge, seismic activity, and the passage of 37 tracers at the RFID stations "*RFID 2*" and "*RFID 3*" during the 2020 season. Notes: Q_c is estimated at 11.9 m^3 s^{-1}. The blue curve indicates log-transformed discharge values reported on the left ordinate axis. Red dots represent log-transformed geophonic activity values reported on the right ordinate axis. Black points indicate tracer passages during the snow-melt and storm-driven floods and are proportional to the virtual velocity. Black horizontal segments indicate the residency period of the tracers within the sensing field of the RFID antennas.

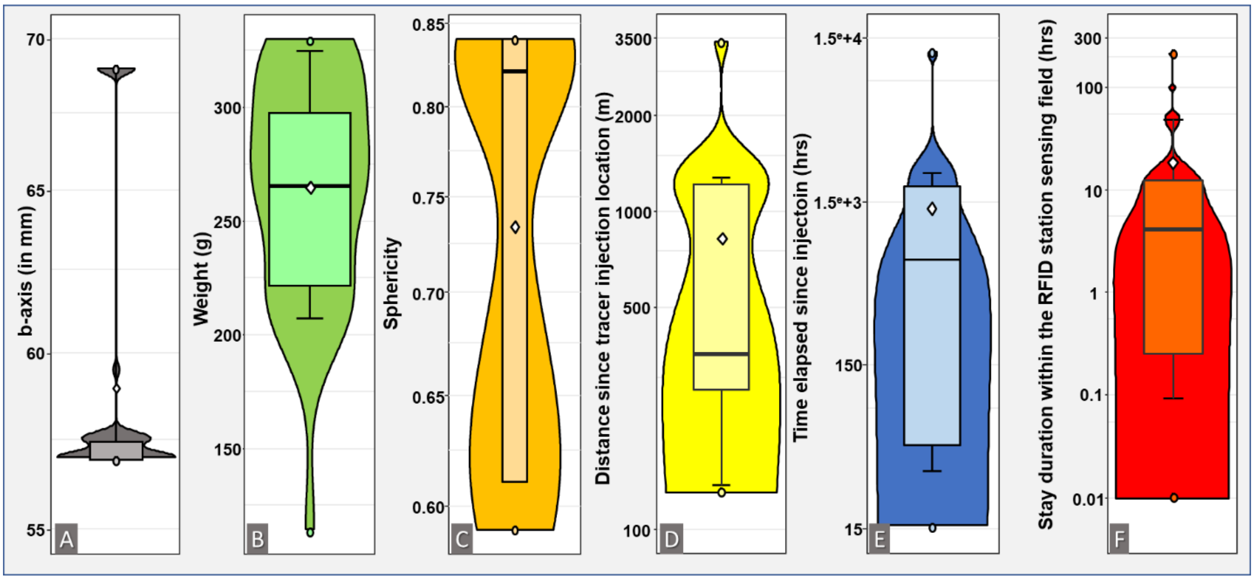

Figure 4. Box-whisker and violin plots of the distributions of the 37 tracer passages recorded: b-axis (A), weight (B), sphericity (C), distance of travel (D), time elapsed since injection before tracer passage at the RFID stations (E), and dwell time in the RFID antenna sensing fields (F). *Notes: whiskers indicate D10 and D90 values. The violin plots' curves indicate the probability density of the entire distribution.*

The values of the RSSI signals recorded over all tracer passages exhibited considerable variation at a time-scale of less than 5 seconds (Figure 5). These variations, which were particularly observed when the tracers had a long residence time within the antenna sensing field and emitted every 0.9 s, were not due to tracer displacement but to multipath propagation of radio frequencies, as previously reported by Cassel et al. (2017). Despite these variations, the use of moving-window temporal averaging allowed the important displacements (significant increase or decrease in average values) and rest periods (levels of average values) to be detected for some of the tracers (Figure 5-A). When the signals of tracers equipped with COIN MOV tags were recorded over a long enough time, it was possible to observe that the significant variations in the RSSI signal (100 observations, which corresponds to a time-window of about 9 s) were mainly concomitant with “moving” indications. To the contrary, the RSSI levels were mainly concomitant with “not moving” indications (Figure 5-A). For the other tracers, those passing though the antenna faster or emitting at the largest time interval, the use of a rolling average function did not allow important displacements and rest periods to be detected (Figure 5-B).

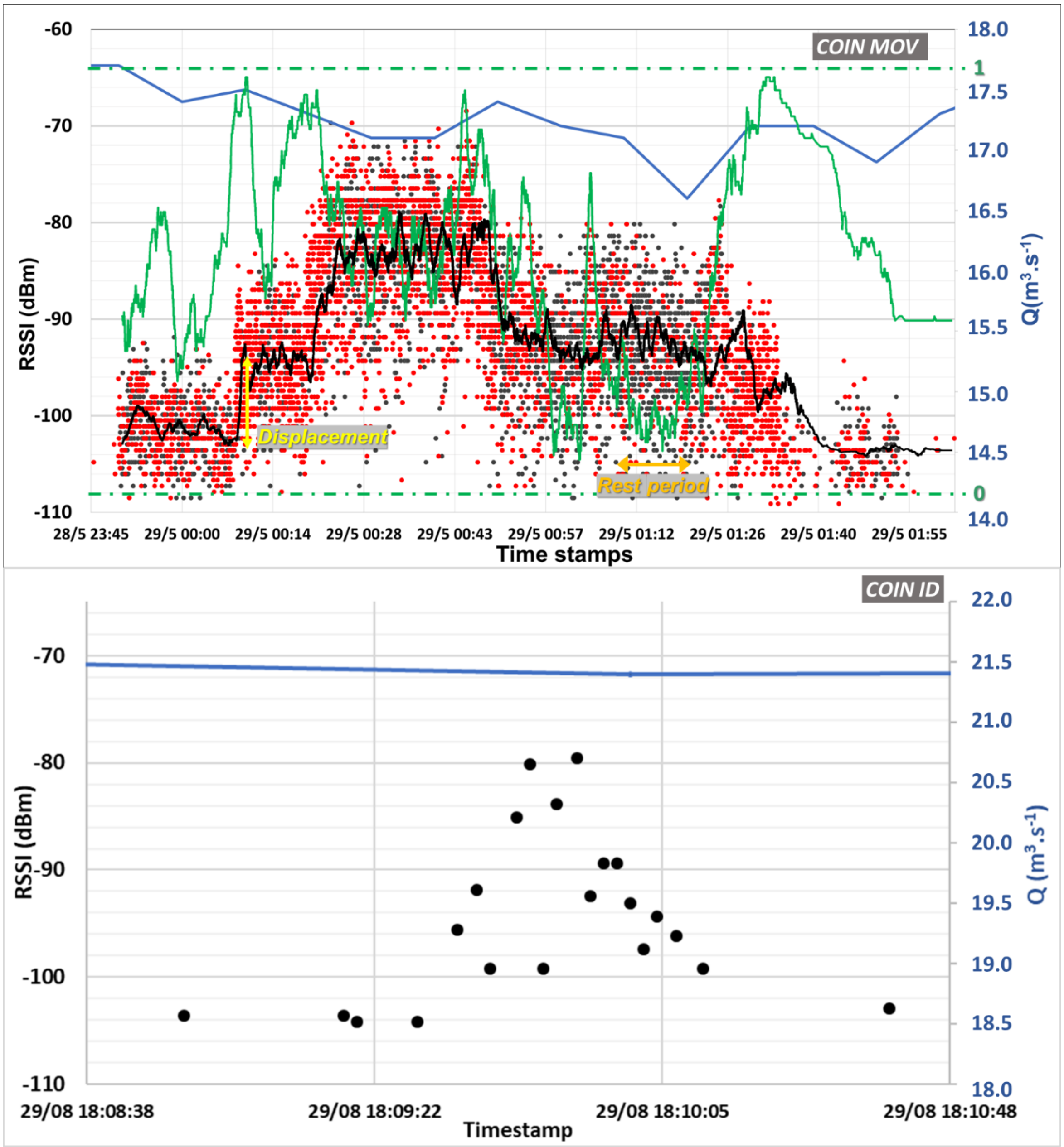

Figure 5. Examples of contrasting RSSI evolutions observed during two tracer passages equipped with different a-UHF tags. *Notes: The COIN MOV and COIN ID tags emitted signals every 900 ms and every 2.2s, respectively, and were sensed over about 2 hours and 2 minutes, respectively. The red and grey points of COIN MOV tags indicate “moving” or “not moving” over the 900-ms period between signal emissions. The dark curve in (A) indicates the rolling average based on 100 observations. The green curve shows the ratio between “moving” and overall detection computed at the same scale as the RSSI rolling average (i.e. 100 observations): the closer to 1 the more mobile, the closer to 0 the less mobile.*

4.2 Virtual particle velocity as a function of a single controlling variable

We found positive power correlations between the tracer virtual velocities and the mean discharges ($R^2 = 0.58$; p-value < 0.001) and dimensionless mean stream power ($R^2 = 0.63$; p-value < 0.001). These correlations are weaker than that between the mean tracer velocities and mean seismic activity ($R^2 = 0.81$; p-value < 0.001; Figure 6). The sum of excess stream power exhibited weak negative power correlations ($R^2 = 0.21$; p-value = 0.83 > 0.05) with tracer virtual velocities. The power law linking tracer virtual velocities to dimensionless mean stream power exhibited a factor (9.7) very close to that of the power law linking tracer virtual velocities to mean seismic activity (9.4). However, its exponent coefficient (4.1) was very close to that of the power law linking mean flow discharges and virtual velocities (4), which is unsurprising, as dimensionless mean stream power is based on mean discharge. Except for the sum of excess stream power, most of the data scattered around the regression curves were for low or high virtual velocity values, whereas dispersion remained relatively moderate for medium values (Figure 6).

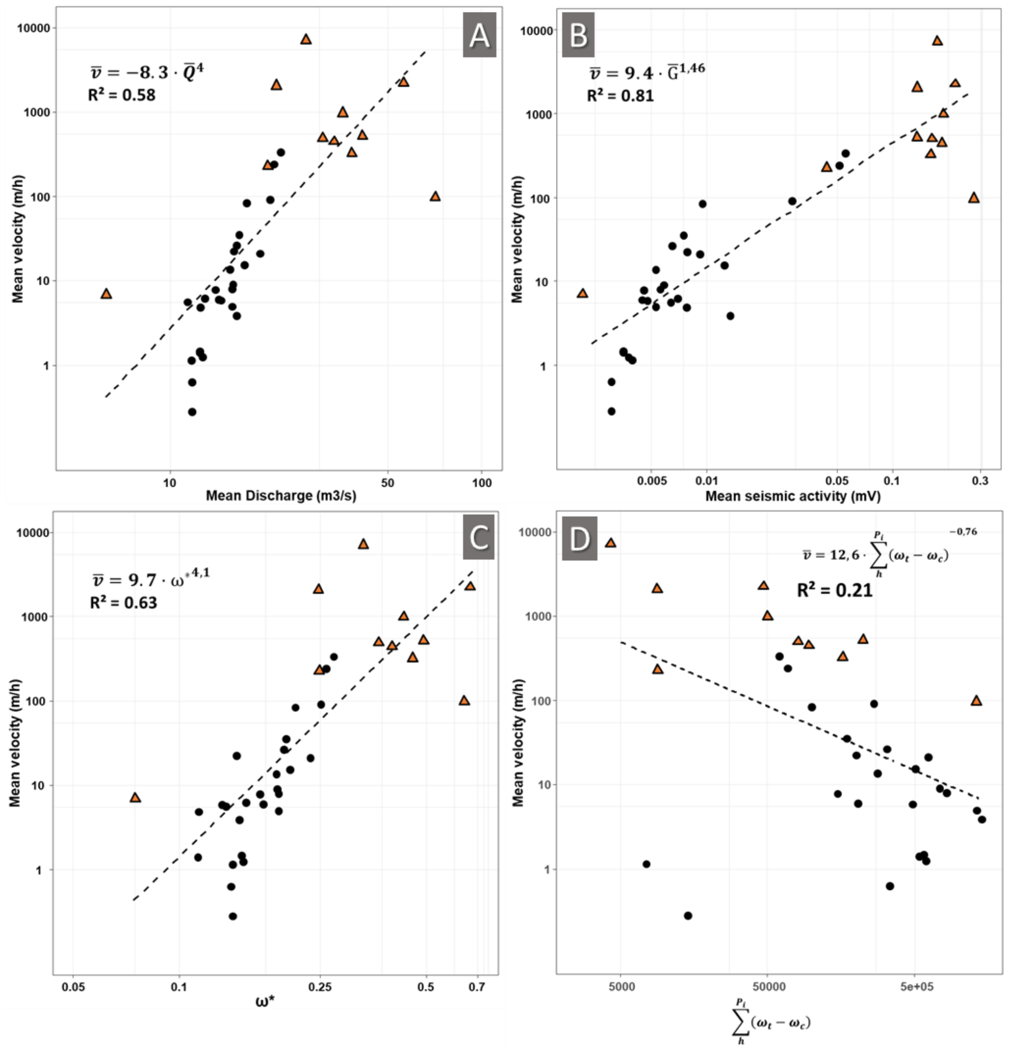

Figure 6. Relationships between tracer virtual velocity and the mean values of (A) flow discharge, (B) seismic activity, (C) dimensionless mean stream-power, and (D) the sum of excess flow power per unit area. *Notes: circles and triangles represent the passages observed during snow-melt events and storm events, respectively.*

The tracer passages occurring during storm events showed higher mean particle velocities, higher flow discharges, and higher seismic activity than those during the snow-melt period (Figure 6). The power regression curves between the tracer virtual velocities ($\boldsymbol{\overline{v}}$) and the mean flow discharges (Figure 6-A), dimensionless mean stream power (Figure 6-C), and average seismic activity (Figure 6-B) show wider dispersion for storm events than during snow-melt periods.

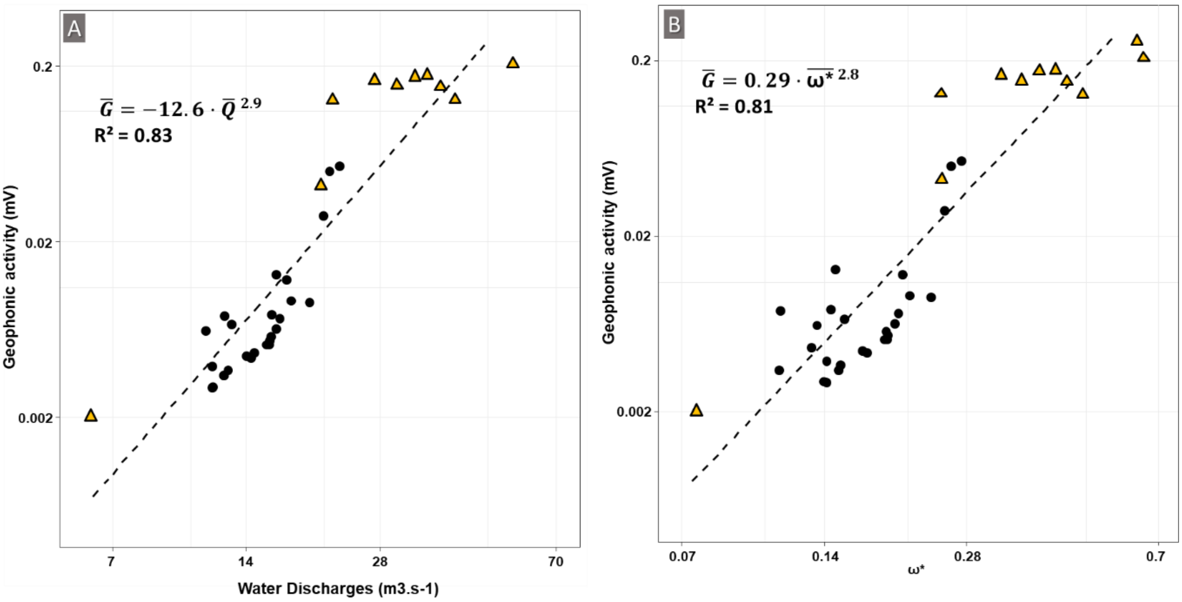

Figure 7. Relationships between mean geophonic activity and (A) mean discharges and (B) dimensionless stream power. *Notes: circles and triangles represent the passages observed during snow-melt events and storm events, respectively*

We also found that averaged seismic activity showed strong positive power correlations with mean flow discharge ($R^2 = 0.83$; *p*-value < 0.001) and dimensionless mean stream power ($R^2 = 0.81$; *p*-value < 0.001; Figure 7), which supports the use of the residuals ($\boldsymbol{\mathcal{E}_i}$) from the power linear model linking log transformed dimensionless mean stream power and log transformed averaged seismic values.

4.3 Multiple regression analysis

Of the eleven controlling variables tested (Table 2), the stepwise procedure identified nine as significant (Table 3). Two of them, $\boldsymbol{\sigma G_i}$ and $\boldsymbol{L_i}$, were less statistically significant, but remained within the 90% confidence interval (*p*-value < 0.1), while a third one, $\boldsymbol{\sigma Q_i}$, was just above the limit (*p*-value = 0.11). Among the six most relevant controlling variables, the most statistically significant (*p*-value < 0.01) were: 1) the dimensionless mean stream power; 2) the residuals from the power model linking dimensionless mean stream power and average seismic activity; and 3) sphericity. These each showed positive coefficients. Meanwhile, the particle weight, range of seismic activity, and time elapsed since injection contributed negatively.

Although the VIF values of $\boldsymbol{t_i}$ (9.6) and $\boldsymbol{L_i}$ (8.6) were both close to 10, all VIF values remained below this limit, indicating that multicollinearity can be dismissed (Table 3).

Table 3. Result of the multiple regression analysis using a stepwise procedure

Variable	Coefficient	p-value	VIF	% of variance explained
Intercept	7.459	4.6e-05 ***		
$\boldsymbol{\mathcal{E}_i}$	1.906	8.3e-08 ***	2.98	18.12
ω^*_i	4.076	3.5e-11 ***	3.46	63.72
$\boldsymbol{\Delta G_i}$	−0.382	2.2e-04 ***	1.51	5.23
$\boldsymbol{\sigma Q_i}$	−0.246	0.113	1.67	1.56
$\boldsymbol{\sigma G_i}$	0.353	0.02 *	3.66	0.31
$\boldsymbol{m_i}$	−2.881	1.6e-03 ***	2.34	0.003
$\boldsymbol{\psi_i}$	5.475	1.2e-05 ***	2.10	4.63
$\boldsymbol{t_i}$	−0.535	3e-03 ***	9.64	1.63
$\boldsymbol{L_i}$	0.532	0.091 *	8.57	0.49

Residual standard error: 0.609 with 28 degrees of freedom. Multiple $R^2 = 0.957$. *Adjusted* $R^2 = 0.943$. *F-statistic: 66.74 with 9 and 27 degrees of freedom. p-value = 4.1e-16.*

**p-value statistically significant at a 90% confidence level*

***p-value statistically significant at a 95% confidence level*

****p-value statistically significant at a 99% confidence level*

The estimated contributions to the variance explained by the independent controlling variables selected by the stepwise procedure again show that the dimensionless mean stream power (ω^*_i) explained 63.7% of variance. The residuals from the power linear model linking dimensionless mean stream power and seismic averaged values ($\mathcal{E}_i$) explained 18.1%. Thus, the sum of these two controlling variables explained 81.8% of the R^2, which is slightly higher than the R^2 (0.816) of the power law linking average seismic activity and tracer virtual velocity. The range of the seismic activity values ($\Delta\boldsymbol{G_i}$) and the standard deviation of these values ($\boldsymbol{\sigma G_i}$) explained 5.2% and 0.31% of the variance, respectively. Thus, the overall virtual velocity variance explained by the seismic data ($\overline{\boldsymbol{G}}_{\mathrm{i}}$, $\Delta\boldsymbol{G_i}$, $\boldsymbol{\sigma G_i}$) was 86.8%. In comparison, the same statistics computed from the flow discharge values explained 69.8% of the tracers' virtual velocity variance. From the tracer properties and past activities tested, the stepwise procedure selected sphericity ($\boldsymbol{\psi_i}$), time elapsed ($\boldsymbol{t_i}$), distance of travel ($\boldsymbol{L_i}$) since injection, and weight ($\boldsymbol{m_i}$), which explained 4.63%, 1.63%, 0.5%, and 0.003% of the virtual velocity variance, respectively. Thus, the tracer b-axis was the single tracer property not selected by the stepwise procedure.

The results of the multiple regression analysis show a highly significant relationship between tracer virtual velocity and the combination of controlling variables ($R^2 = 0.957$; *p*-value < 0.001). The data scattering around the 1:1 line is moderate and relatively homogeneous between low, medium, and high virtual velocity values (Figure 7). Equation 1 (E1) was adapted to estimate the tracers' virtual velocity observed within the studied reach for both storm events and snow-melt events (Figure 8).

$$\boldsymbol{\overline{v} = 7.46} \cdot \boldsymbol{\mathcal{E}_i}^{\mathbf{1.91}} \cdot \omega^{*}{}_{\boldsymbol{i}}^{\mathbf{4.08}} \cdot \Delta\boldsymbol{G_i}^{\mathbf{-0.38}} \cdot \boldsymbol{\sigma Q_i}^{\mathbf{-0.25}} \cdot \boldsymbol{\sigma G_i}^{\mathbf{0.35}} \qquad \textbf{(E4)}$$

$$\cdot\, \boldsymbol{m_i}^{\mathbf{-2.88}} \cdot \boldsymbol{\psi_i}^{\mathbf{5.47}} \cdot \boldsymbol{t_i}^{\mathbf{-0.54}} \cdot \boldsymbol{L_i}^{\mathbf{0.53}}$$

Of the 37 values modelled, all were within an order of magnitude of the observed values, and only seven were found to deviate by more than a factor of two.

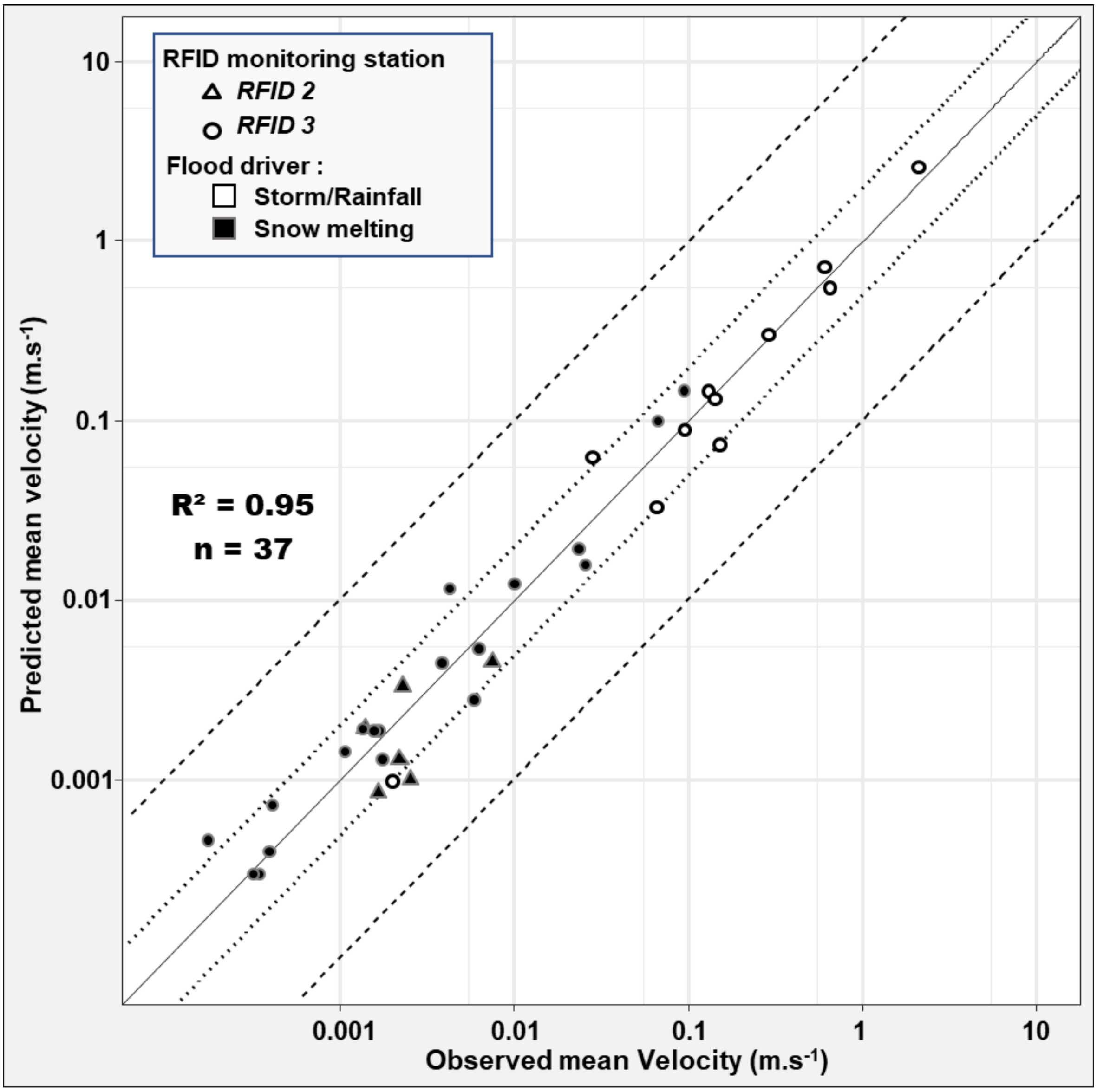

Figure 8. Comparison between the observed and predicted virtual velocity of tracer passages.

Notes: dashed and dotted lines indicate the 10- and 2-fold intervals respectively.

5. Discussion

About the observations and monitoring

The virtual velocities reported in this study ranged between 0.29 and 7548 m h^{-1}, with mean and median values of 440 and 15.7 m h^{-1}, respectively. Most of these values are in the range of those observed on comparable river systems by Misset et al. (2020), but at larger temporal and spatial scales, with the authors reporting virtual velocities between 13 and 27 m h^{-1} on a "braided-confined-braided" sequence of the Séveraisse River, while Liébault et al. (2012) reported values of about 100 m h^{-1} for several of the grain sizes monitored in a wandering mountain stream. However, the virtual velocities reported in this paper are higher than those observed on the alpine headwater streams of the Rio Cordon, where virtual velocities were globally inferior to 6 m h^{-1} (Mao et al., 2017; Rainato et al., 2020; Oss Cazzador et al., 2021). Although our observations are higher than that, they are globally inferior to the 60 m h^{-1} reported by Dell'Agnese et al. (2015), who also reported that higher virtual velocity was associated more with rainfall-dominated periods than with snowmelt and mixed periods.

The fastest virtual velocity we monitored over a distance of 60 m was 2.01 m s^{-1}, a value consistent with that reported by Habersack (2001) on a braided reach of the Waimakariri River in New Zealand, who observed a maximum instantaneous particle velocity of 2 m s^{-1} and a maximal individual step length of 24.9 m. It is reasonable to hypothesize that the geometry of the straight confined channel of our study site allowed for a longer individual step length compared with that generally observed on a braided reach. The tracer virtual velocity value is also consistent with the flow velocity of 2.7 m s^{-1} estimated at the mean discharge value of 27 m^3 s^{-1} measured during its passage.

The estimated critical discharge for bedload transport ($\boldsymbol{Q_c}$) is ca. 11.9 m^3 s^{-1}. This value is consistent with the tracer passages observed in the early stage of the snow melt season up until the flood events of the 1st and 2nd July, whose peak flow discharges reached 28 m^3 s^{-1} and 21.5 m^3 s^{-1}, respectively (Figure 3). Prior to these flood events, the tracers passing through the station sensing field at average discharge values ($\boldsymbol{\overline{Q}}_\mathrm{i}$) very close to $\boldsymbol{Q_c}$ (*i.e.* from 11.6 to 12.7 m^3 s^{-1}) exhibited the lowest virtual velocities (from 0.29 to 1.5 m h^{-1}). After the 1st–2nd July flood events, this threshold was no longer so clear. Indeed, the tracers that passed through the station sensing field at $\boldsymbol{\overline{Q}}_\mathrm{i} \approx \boldsymbol{Q_c}$ exhibited more varied residence times within the antenna sensing field (*i.e.* 9.6, 11.1, 12.4, and 53 hours) and exhibited three-times higher $\boldsymbol{\overline{v}}$ values (*i.e.* 6.3, 5.7, 4.9, and 1.2 m h^{-1}, respectively) at equivalent $\boldsymbol{\overline{Q}}_\mathrm{i}$ values (*i.e.* 12.9, 11.3, 12.4, and 11.6 m^3 s^{-1}, respectively) than the tracers monitored before the 1st–2nd July flood events. Over the post-flood-event period, there was a temporary increase in seismic activity that lasted until 6th July, although flow discharges were slightly lower than in the pre-flood-event period (Figure 3). These observations highlight the role of the antecedent conditions on tracer passage dynamics. Indeed, breaking of the armor layer, channel shifting (especially in river systems as dynamic as braided streams), or ongoing channel adjustment after a major flood can locally and temporarily promote bedload particle transport. Such delayed bedload transport processes following a flood event were reported by Aigner et al. (2017) using a geophone plate, but remain difficult to observe with sediment tracers, although they demonstrate the complementarity of geophones and tracer tools. This is an important topic that could bring elements for understanding the passage of tracers observed at the lowest average discharge value $\overline{\boldsymbol{Q}}_{\mathrm{i}}$ = 6.2 m^3 s^{-1}, which is well below the $\boldsymbol{Q_c}$**,** but still at a virtual velocity of $\overline{\boldsymbol{v}}$ = 7.3 m h^{-1}.

The differences in time interval between signal emissions and the residence time within the antenna sensing field caused the patterns of RSSI signals recorded during tracer passages to be very different in resolution (Figure 5). Thus, the step lengths of displacements and the durations of rest periods could not be compared. To achieve such an objective, the experimentation set up would need to focus on short-term measurements and the transponders would need to be programmed to emit at shorter time intervals to improve signal temporal resolution and the recording of numerous detections, rather than focusing on an extend emission interval and transponder lifespan. The use of several stations installed alongside each other would extend the channel length monitored, improve the signal recording resolution, and could even allow 3D reconstruction of the travel path.

About drivers and virtual mobility prediction

Although Figure 6-D shows a marked segregation relative to flood event types, the statistical relationship between the sum of excess stream power and virtual velocities exhibited weak negative power correlations ($R^2 = 0.21$; p-value = 0.83 > 0.05). This negative correlation, consistent with previous work by Chardon et al. (2021), is due to the fact that both virtual velocity and cumulative excess stream power are dependent on time, but the first is negatively correlated (*i.e.* the shorter the time spent in the antenna sensing field, the higher the virtual velocity) while the second is positively correlated (*i.e.* the longer the time spent, the higher the cumulative excess stream power). Thus, cumulative excess stream power is more suitable for investigating transport distance than for investigating virtual velocity.

Furthermore, the percentage of mean tracer velocity variance explained by the seismic signals was higher than that explained by flow discharges (Figure 6-A and -B). Both are strongly correlated (Figure 7), and geophone activity integrates some of the virtual velocity variance explained by flow discharge. Thus, compared with the single flow discharge, the seismic signal, as an integrated measure of flow conditions and bedload transport, offers a better way to predict the virtual velocity of mobile coarse particles during bedload processes in a confined channel. The link between virtual velocity and seismic signal is consistent with the results of Schneider et al. (2014), who reported a strong link between unit bed load volume and the mean distance of tracer transport. Their results and those we report here support the use of tracers, together with measurements of the scour layer thickness made by classical or RFID scour chains (Laronne et al., 1994; Liébault and Laronne, 2008; Brenna et al., 2019; Melun et al., 2019; Boutault, 2020), to quantify bedload transport flux in rivers where direct sampling is not feasible.

The overall variance of mean tracer velocities explained by particle properties and past activity was 6.8%, most of it being explained by sphericity, which is consistent with previous in-flume tracking experiments (Cassel et al., 2021a), while the *b*-axis was not significant in the stepwise procedure. It would be tempting to think that sphericity has a bigger influence on the virtual velocity of coarse particles. However, the small variability in the b-axis values and its inclusion in the dimensionless stream power formula could have reduced its contribution to explaining the virtual velocity variance. Our use of dimensionless mean stream power, which includes *b*-axis in its formula, instead of flow discharge, was verified. Furthermore, the use of $\overline{\boldsymbol{Q}}_{\mathrm{i}}$ in the stepwise procedure instead of $\omega^{*}{}_{\mathbf{i}}$ did not change *b*-axis non-selection, nor the final R² of the final multiple regression model. However, the particle weight, which was also tested in this study and correlated with *b*-axis, presented a greater range of values but explained very little of the mean tracer velocity variance (Table 3). The time elapsed and distance of travel since tracer injection explained small percentages of variance: 1.6% and 0.5%, respectively. They had almost the same absolute coefficient value, but that of the time elapsed was negative, while that of the distance of travel was positive.

Finally, future work should investigate and compare the coefficients for the controlling variables resulting from the multiple regression analysis with those obtained in river systems of contrasting morphologies. Indeed, it is reasonable to assume that in river systems exhibiting less torrential processes, the proportion of particle virtual velocity variance explained by the seismic activity signal could be lower, whereas that of the unit stream power could be higher. Further comparisons are needed to determine if such methodology would allow assessment of whether or not the interactions between moving particles influence their mobility (entrainment, motion, deposition), and to what extent compared with flow discharge.

Conclusions

The e-RFIDuino station showed good efficiency for monitoring the passage of tracers in a diversity of flood events and associated hydraulic conditions. It also has important potential for the study of the phases of bedload transport at the particle scale. The combination of RFID and geophone environmental stations allowed surveying of tracer passages and seismic activity over a period of several months and detection of shifts in river system dynamics in pre- and post-flood analyses. The comparison of the efficiencies of flow discharge and seismic activity for predicting the virtual velocity of tracers showed that seismic activity, as for suspended load prediction Misset et al. (2020b), is a better controlling factor than flow discharge. The results of the multiple regression analysis also confirmed, in-river, the contribution of the particle shape on the observed virtual velocity. Further investigations in different river systems with finer granulometry and/or a larger channel and/or more fluvial and less torrential dynamics are needed to specify the potential of such a monitoring set up and to achieve insights into the relationships between grain scale processes and bulk bedload transport.

Acknowledgments

The authors thank the electricity company Électricité de France (EDF), who provided us with the discharge values measured at its gauging station. Léonie Besson and Nils Dumarski are acknowledged for their participation in the e-RFIDuino station installation and sensing field delineation during field campaigns. The authors thank Karl Embleton for his proofreading work.

This work was partially funded by the **LabEx DRIIHM** French program "Investissements d'Avenir" (ANR-11-LABX-0010) managed by the ANR. It was supported by the OHM Vallée du Rhône.

This work was performed within the framework of the EUR H2O'Lyon (ANR-17-EURE-0018) of Université de Lyon, part of the program "Investissements d'Avenir" (ANR-11-IDEX-0007) operated by the French National Research Agency (ANR).

This work was carried out as part of the project **Greendam,** which is an original partnership integrating an inter-disciplinary scientific group (EVS UMR 5600 and SiSyPh UMR5672 du CNRS et INRAE), a large electricity producer (Électricité de France - EDF), and a local SME (GeoPeka), as part of a partnership project with the Région Auvergne-Rhône-Alpes.

Declaration of interests

The authors declare no competing interests.

Human and animal rights

The authors declare that no human or animal subjects were used in this study.

References

Aigner J, Kreisler A, Rindler R, Hauer C, Habersack H. 2017. Bedload pulses in a hydropower affected alpine gravel bed river. Geomorphology **291** : 116–127. DOI: 10.1016/j.geomorph.2016.05.015

Ancey C. 2020a. Bedload transport: a walk between randomness and determinism. Part 1. The state of the art. Journal of Hydraulic Research **58** : 1–17. DOI: 10.1080/00221686.2019.1702594

Ancey C. 2020b. Bedload transport: a walk between randomness and determinism. Part 2. Challenges and prospects. Journal of Hydraulic Research **58** : 18–33. DOI: 10.1080/00221686.2019.1702595

Antoniazza G, Nicollier T, Wyss CR, Boss S, Rickenmann D. 2020. Bedload Transport Monitoring in Alpine Rivers: Variability in Swiss Plate Geophone Response. Sensors **20** : 4089. DOI: 10.3390/s20154089

Arnaud F, Piégay H, Béal D, Collery P, Vaudor L, Rollet A-J. 2017. Monitoring gravel augmentation in a large regulated river and implications for process-based restoration. Earth Surface Processes and Landforms **42** : 2147–2166. DOI: 10.1002/esp.4161

Bagnold RA. 1966. An approach to the sediment transport problem from general physics . USGS Numbered Series. U. S. Govt. Print. Off., [online] Available from: http://pubs.er.usgs.gov/publication/pp422I (Accessed 21 November 2018)

Bagnold RA. 1980. An Empirical Correlation of Bedload Transport Rates in Flumes and Natural Rivers. Proceedings of the Royal Society A: Mathematical, Physical and Engineering Sciences **372** : 453–473. DOI: 10.1098/rspa.1980.0122

Bakker M, Gimbert F, Geay T, Misset C, Zanker S, Recking A. 2020. Field Application and Validation of a Seismic Bedload Transport Model. Journal of Geophysical Research: Earth Surface **125** DOI: 10.1029/2019JF005416 [online] Available from: https://onlinelibrary.wiley.com/doi/10.1029/2019JF005416 (Accessed 4 February 2021)

Bel C, Liébault F, Navratil O, Eckert N, Bellot H, Fontaine F, Laigle D. 2017. Rainfall control of debris-flow triggering in the Réal Torrent, Southern French Prealps. Geomorphology **291** : 17–32. DOI: 10.1016/j.geomorph.2016.04.004

Boutault F. 2020. Etude de l’impact cumulé des facteurs d’anthropisation sur la Dordogne moyenne et préconisations en vue d’une restauration écologique du cours d’eau, These en préparation, Lyon [online] Available from: http://www.theses.fr/s253415 (Accessed 16 February 2021)

Bradley DN. 2017. Direct Observation of Heavy-Tailed Storage Times of Bed Load Tracer Particles Causing Anomalous Superdiffusion. Geophysical Research Letters **44** : 12,227-12,235. DOI: https://doi.org/10.1002/2017GL075045

Brenna A, Surian N, Mao L. 2019. Virtual Velocity Approach for Estimating Bed Material Transport in Gravel-Bed Rivers: Key Factors and Significance. Water Resources Research **55** : 1651–1674. DOI: 10.1029/2018WR023556

Brousse G, Arnaud-Fassetta G, Liébault F, Bertrand M, Melun G, Loire R, Malavoi J, Fantino G, Borgniet L. 2020a. Channel response to sediment replenishment in a large gravel-bed river: The case of the Saint-Sauveur dam in the Buëch River (Southern Alps, France). River Research and Applications : rra.3527. DOI: 10.1002/rra.3527

Brousse G, Liébault F, Arnaud-Fassetta G, Breilh B, Tacon S. 2020b. Gravel replenishment and active-channel widening for braided-river restoration: The case of the Upper Drac River (France). Science of The Total Environment : 142517. DOI: 10.1016/j.scitotenv.2020.142517

Cassel M, Dépret T, Piégay H. 2017. Assessment of a new solution for tracking pebbles in rivers based on active RFID: a new solution for tracking pebbles in rivers based on active RFID. Earth Surface Processes and Landforms **42** : 1938–1951. DOI: 10.1002/esp.4152

Cassel M, Lavé J, Recking A, Malavoi J-R, Piégay H. 2021a. Bedload transport in rivers, size matters but so does shape. Scientific Reports **11** : 1–11. DOI: 10.1038/s41598-020-79930-7

Cassel M, Navratil O, Perret F, Piégay H. 2021b. The e-RFIDuino: An Arduino-based RFID environmental station to monitor mobile tags. HardwareX **10** : e00210. DOI: 10.1016/j.ohx.2021.e00210

Cassel M, Piégay H, Fantino G, Lejot J, Bultingaire L, Michel K, Perret F. 2020. Comparison of ground-based and UAV a-UHF artificial tracer mobility monitoring methods on a braided river. Earth Surface Processes and Landforms : esp.4777. DOI: 10.1002/esp.4777

Cassel M, Piégay H, Lavé J. 2016. Effects of transport and insertion of radio frequency identification (RFID) transponders on resistance and shape of natural and synthetic pebbles: applications for riverine and coastal bedload tracking: Transport and Rfid-Insertion Effects on the Fragility of Pebbles. Earth Surface Processes and Landforms DOI: 10.1002/esp.3989 [online] Available from: http://doi.wiley.com/10.1002/esp.3989 (Accessed 4 August 2016)

Chapuis M, Dufour S, Provansal M, Couvert B, de Linares M. 2015. Coupling channel evolution monitoring and RFID tracking in a large, wandering, gravel-bed river: Insights into sediment routing on geomorphic continuity through a riffle–pool sequence. Geomorphology **231** : 258–269. DOI: 10.1016/j.geomorph.2014.12.013

Chardon V, Schmitt L, Arnaud F, Piégay H, Clutier A. 2021. Efficiency and sustainability of gravel augmentation to restore large regulated rivers: Insights from three experiments on the Rhine River (France/Germany). Geomorphology **380** : 107639. DOI: 10.1016/j.geomorph.2021.107639

Cook KL, Andermann C, Gimbert F, Adhikari BR, Hovius N. 2018. Glacial lake outburst floods as drivers of fluvial erosion in the Himalaya. Science **362** : 53–57. DOI: 10.1126/science.aat4981

Dell'Agnese A, Brardinoni F, Toro M, Mao L, Engel M, Comiti F. 2015. Bedload transport in a formerly glaciated mountain catchment constrained by particle tracking. Earth Surface Dynamics **3** : 527–542. DOI: 10.5194/esurf-3-527-2015

Dietze M, Lagarde S, Halfi E, Laronne JB, Turowski JM. 2019. Joint Sensing of Bedload Flux and Water Depth by Seismic Data Inversion. Water Resources Research **55** : 9892–9904. DOI: 10.1029/2019WR026072

Dietze M, Losee J, Polvi L, Palm D. 2020. A seismic monitoring approach to detect and quantify river sediment mobilization by steelhead redd-building activity. Earth Surface Processes and Landforms **45** : 2840–2849. DOI: https://doi.org/10.1002/esp.4933

Eaton BC, Church M. 2011. A rational sediment transport scaling relation based on dimensionless stream power. Earth Surface Processes and Landforms **36** : 901–910. DOI: 10.1002/esp.2120

Einstein H. 1937. Bed load transport as a probability problem. Shen H (ed). : 1–105.

Ergenzinger P, Schmidt KH. 1990. Stochastic elements of bed load transport in a steppool mountain river. Hydrology in mountainous regions. II—Artificial reservoirs, water and slopes: International Association of Hydrological Sciences Publication **194** : 39–46.

Frey P, Church M. 2011. Bedload: a granular phenomenon. Earth Surface Processes and Landforms **36** : 58–69. DOI: 10.1002/esp.2103

Gilet L, Gob F, Gautier E, Houbrechts G, Virmoux C, Thommeret N. 2020. Hydro-morphometric parameters controlling travel distance of pebbles and cobbles in three gravel bed streams. Geomorphology : 107117. DOI: 10.1016/j.geomorph.2020.107117

Gimbert F, Fuller BM, Lamb MP, Tsai VC, Johnson JPL. 2019. Particle transport mechanics and induced seismic noise in steep flume experiments with accelerometer-embedded tracers. Earth Surface Processes and Landforms **44** : 219–241. DOI: 10.1002/esp.4495

Habersack H, Seitz H, Liedermann M. 2010. Integrated automatic bedload transport monitoring. US Geological Survey Scientific Investigations Report **5091** : 218–235.

Habersack HM. 2001. Radio-tracking gravel particles in a large braided river in New Zealand: A field test of the stochastic theory of bed load transport proposed by Einstein. Hydrological Processes **15** : 377–391.

Haschenburger JK. 2013. Tracing river gravels: Insights into dispersion from a long-term field experiment. Geomorphology **200** : 121–131. DOI: 10.1016/j.geomorph.2013.03.033

Haschenburger JK, Church M. 1998. Bed material transport estimated from the virtual velocity of sediment. Earth Surface Processes and Landforms **23** : 791–808. DOI: 10.1002/(SICI)1096-9837(199809)23:9<791::AID-ESP888>3.0.CO;2-X

Hassan MA, Bradley DN. 2017. Geomorphic Controls on Tracer Particle Dispersion in Gravel-Bed Rivers. In Gravel-Bed Rivers , Tsutsumi D and Laronne JB (eds). John Wiley & Sons, Ltd: Chichester, UK; 159–184. [online] Available from: http://doi.wiley.com/10.1002/9781118971437.ch6 (Accessed 29 April 2020)

Hassan MA, Roy AG. 2016. Coarse particle tracing in fluvial geomorphology. In Tools in Fluvial Geomorphology , Kondolf G thias and Piégay H (eds). John Wiley & Sons, Ltd; 306–323. [online] Available from: http://onlinelibrary.wiley.com/doi/10.1002/9781118648551.ch14/summary (Accessed 2 November 2016)

Houbrechts G, Levecq Y, Peeters A, Hallot E, Van Campenhout J, Denis A-C, Petit F. 2015. Evaluation of long-term bedload virtual velocity in gravel-bed rivers (Ardenne, Belgium). Geomorphology **251** : 6–19. DOI: 10.1016/j.geomorph.2015.05.012

Imhoff KS, Wilcox AC. 2016. Coarse bedload routing and dispersion through tributary confluences. Earth Surface Dynamics **4** : 591–605. DOI: 10.5194/esurf-4-591-2016

James G, Witten D, Hastie T, Tibshirani R. 2013. An Introduction to Statistical Learning: with Applications in R . Springer-Verlag: New York [online] Available from: https://www.springer.com/gp/book/9781461471370 (Accessed 10 March 2021)

Kondolf GM, Piégay H. 2016. Tools in fluvial geomorphology: problem statement and recent practice. In Tools in Fluvial Geomorphology , Kondolf G thias and Piégay H (eds). John Wiley & Sons, Ltd; 1–12. [online] Available from: http://onlinelibrary.wiley.com/doi/10.1002/9781118648551.ch1/summary (Accessed 2 November 2016)

Lamarre H, Roy AG. 2008. The role of morphology on the displacement of particles in a step–pool river system. Geomorphology **99** : 270–279. DOI: 10.1016/j.geomorph.2007.11.005

Laronne JB, Outhet DN, Carling PA, McCabe TJ. 1994. Scour chain employment in gravel bed rivers. CATENA **22** : 299–306. DOI: 10.1016/0341-8162(94)90040-X

Liébault F, Bellot H, Chapuis M, Klotz S, Deschâtres M. 2012. Bedload tracing in a high-sediment-load mountain stream: bedload tracing in a high-sediment-load mountain stream. Earth Surface Processes and Landforms **37** : 385–399. DOI: 10.1002/esp.2245

Liébault F, Laronne JB. 2008. Evaluation of bedload yield in gravel-bed rivers using scour chains and painted tracers: the case of the Esconavette Torrent (Southern French Prealps). Geodinamica Acta **21** : 23–34. DOI: 10.3166/ga.21.23-34

Mao L, Dell'Agnese A, Comiti F. 2017. Sediment motion and velocity in a glacier-fed stream. Geomorphology **291** : 69–79. DOI: 10.1016/j.geomorph.2016.09.008

Melun G et al. 2019. Dossier : L'hydromorphologie. La Houille Blanche : 5–25. DOI: 10.1051/lhb/2019037

Milan DJ. 2013. Virtual velocity of tracers in a gravel-bed river using size-based competence duration. Geomorphology **198** : 107–114. DOI: 10.1016/j.geomorph.2013.05.018

Misset C et al. 2020a. Combining multi-physical measurements to quantify bedload transport and morphodynamics interactions in an Alpine braiding river reach. Geomorphology **351** : 106877. DOI: 10.1016/j.geomorph.2019.106877

Misset C, Recking A, Legout C, Bakker M, Gimbert F, Geay T, Zanker S. 2020b. Using continuous turbidity and seismic measurements to unravel sediment provenance and interaction between suspended and bedload transport in an Alpine catchment. Geophysical Research Letters DOI: 10.1029/2020GL090696 [online] Available from: https://onlinelibrary.wiley.com/doi/10.1029/2020GL090696 (Accessed 14 January 2021)

Navratil O, Liébault F, Bellot H, Travaglini E, Theule J, Chambon G, Laigle D. 2013. High-frequency monitoring of debris-flow propagation along the Réal Torrent, Southern French Prealps. Geomorphology **201** : 157–171. DOI: 10.1016/j.geomorph.2013.06.017

Olinde L, Johnson J. 2015. Using RFID and accelerometer-embedded tracers to measure probabilities of bed load transport, step lengths, and rest times in a mountain stream. Water Resour. Res. **51** : 7572–7589. DOI: 10.1002/2014wr016120

Oss Cazzador D, Rainato R, Mao L, Martini L, Picco L. 2021. Coarse sediment transfer and geomorphic changes in an alpine headwater stream. Geomorphology **376** : 107569. DOI: 10.1016/j.geomorph.2020.107569

Phillips CB, Jerolmack DJ. 2014. Dynamics and mechanics of bed-load tracer particles. Earth Surface Dynamics **2** : 513–530. DOI: 10.5194/esurf-2-513-2014

Phillips CB, Martin RL, Jerolmack DJ. 2013. Impulse framework for unsteady flows reveals superdiffusive bed load transport. Geophysical Research Letters **40** : 1328–1333. DOI: 10.1002/grl.50323

Rainato R, Mao L, Picco L. 2020. The effects of low-magnitude flow conditions on bedload mobility in a steep mountain stream. Geomorphology **367** : 107345. DOI: 10.1016/j.geomorph.2020.107345

Rickenmann D et al. 2014. Bedload transport measurements with impact plate geophones: comparison of sensor calibration in different gravel-bed streams: IMPACT PLATE GEOPHONE CALIBRATION. Earth Surface Processes and Landforms **39** : 928–942. DOI: 10.1002/esp.3499

Rickenmann D. 2017. Bed-Load Transport Measurements with Geophones and Other Passive Acoustic Methods. Journal of Hydraulic Engineering **143** : 03117004. DOI: 10.1061/(ASCE)HY.1943-7900.0001300

Rickenmann D, Turowski JM, Fritschi B, Klaiber A, Ludwig A. 2012. Bedload transport measurements at the Erlenbach stream with geophones and automated basket samplers: BEDLOAD TRANSPORT MEASUREMENTS IN THE ERLENBACH. Earth Surface Processes and Landforms **37** : 1000–1011. DOI: 10.1002/esp.3225

Roth DL, Finnegan NJ, Brodsky EE, Rickenmann D, Turowski JM, Badoux A, Gimbert F. 2017. Bed load transport and boundary roughness changes as competing causes of hysteresis in the relationship between river discharge and seismic amplitude recorded near a steep mountain stream. Journal of Geophysical Research: Earth Surface **122** : 1182–1200. DOI: https://doi.org/10.1002/2016JF004062

Schmandt B, Gaeuman D, Stewart R, Hansen SM, Tsai VC, Smith J. 2017. Seismic array constraints on reach-scale bedload transport. Geology **45** : 299–302. DOI: 10.1130/G38639.1

Schneider J, Hegglin R, Meier S, Turowski J, Nitsche M, Rickenmann D. 2010. Studying sediment transport in mountain rivers by mobile and stationary RFID antennas. In River Flow 2010: Proceedings of the 5th International Conference on Fluvial Hydraulics , . Dittrich, K., Koll, A., Aberle, J., and Geisen- hainer, P., Bundesanstalt: Braunschweig, Germany; 1723—1730.

Schneider JM, Turowski JM, Rickenmann D, Hegglin R, Arrigo S, Mao L, Kirchner JW. 2014. Scaling relationships between bed load volumes, transport distances, and stream power in steep mountain channels: Tracer Erlenbach. Journal of Geophysical Research: Earth Surface **119** : 533–549. DOI: 10.1002/2013JF002874

Schumm SA, Stevens MA. 1973. Abrasion in Place: A Mechanism for Rounding and Size Reduction of Coarse Sediments in Rivers. Geology **1** : 37. DOI: 10.1130/0091-7613(1973)1<37:AIPAMF>2.0.CO;2

Shields A. 1936. Anwendung der Aehnlichkeitsmechanik und der Turbulenzforschung auf die Geschiebebewegung. PhD Thesis Technical University Berlin [online] Available from: https://repository.tudelft.nl/islandora/object/uuid:61a19716-a994-4942-9906-f680eb9952d6?collection=research (Accessed 13 September 2017)

Sneed ED, Folk RL. 1958. Pebbles in the Lower Colorado River, Texas a Study in Particle Morphogenesis. The Journal of Geology **66** : 114–150.

Stähly S, Franca MJ, Robinson CT, Schleiss AJ. 2020. Erosion, transport and deposition of a sediment replenishment under flood conditions. Earth Surface Processes and Landforms **45** : 3354–3367. DOI: 10.1002/esp.4970

Stevens MA. 1969. Scour in riprap at culvert outlets, Colorado State University: Fort Collins

Strickler A. 1923. Beiträge zur Frage der Geschwindigkeitsformel und der Rauhigkeitszahlen für Ströme, Kanäle und geschlossene Leitungen

Tsai VC, Minchew B, Lamb MP, Ampuero J-P. 2012. A physical model for seismic noise generation from sediment transport in rivers: SEISMIC NOISE FROM SEDIMENT TRANSPORT. Geophysical Research Letters **39** : n/a-n/a. DOI: 10.1029/2011GL050255

Urbonas BR. 1968. Forces on a bed particle in a dumped rock stilling basin, Colorado State University: Fort Collins

Vázquez-Tarrío D, Batalla RJ. 2019. Assessing Controls on the Displacement of Tracers in Gravel-Bed Rivers. Water **11** : 1598. DOI: 10.3390/w11081598

Vázquez-Tarrío D, Recking A, Liébault F, Tal M, Menéndez-Duarte R. 2018. Particle transport in gravel-bed rivers: revisiting passive tracer data: Particle transport in gravel-bed rivers. Earth Surface Processes and Landforms DOI: 10.1002/esp.4484 [online] Available from: http://doi.wiley.com/10.1002/esp.4484 (Accessed 31 August 2018)